

Measurements of All-Particle Energy Spectrum and Mean Logarithmic Mass of Cosmic Rays from 0.3 to 30 PeV with LHAASO-KM2A

Zhen Cao,^{1,2,3} F. Aharonian,^{4,5} Axikegu,⁶ Y.X. Bai,^{1,3} Y.W. Bao,⁷ D. Bastieri,⁸ X.J. Bi,^{1,2,3} Y.J. Bi,^{1,3} W. Bian,⁹ A.V. Bukevich,¹⁰ Q. Cao,¹¹ W.Y. Cao,¹² Zhe Cao,^{13,12} J. Chang,¹⁴ J.F. Chang,^{1,3,13} A.M. Chen,⁹ E.S. Chen,^{1,2,3} H.X. Chen,¹⁵ Liang Chen,¹⁶ Lin Chen,⁶ Long Chen,⁶ M.J. Chen,^{1,3} M.L. Chen,^{1,3,13} Q.H. Chen,⁶ S. Chen,¹⁷ S.H. Chen,^{1,2,3} S.Z. Chen,^{1,3} T.L. Chen,¹⁸ Y. Chen,⁷ N. Cheng,^{1,3} Y.D. Cheng,^{1,2,3} M.Y. Cui,¹⁴ S.W. Cui,¹¹ X.H. Cui,¹⁹ Y.D. Cui,²⁰ B.Z. Dai,¹⁷ H.L. Dai,^{1,3,13} Z.G. Dai,¹² Danzengluobu,¹⁸ X.Q. Dong,^{1,2,3} K.K. Duan,¹⁴ J.H. Fan,⁸ Y.Z. Fan,¹⁴ J. Fang,¹⁷ J.H. Fang,¹⁵ K. Fang,^{1,3} C.F. Feng,²¹ H. Feng,¹ L. Feng,¹⁴ S.H. Feng,^{1,3} X.T. Feng,²¹ Y. Feng,¹⁵ Y.L. Feng,¹⁸ S. Gabici,²² B. Gao,^{1,3} C.D. Gao,²¹ Q. Gao,¹⁸ W. Gao,^{1,3} W.K. Gao,^{1,2,3} M.M. Ge,¹⁷ L.S. Geng,^{1,3} G. Giacinti,⁹ G.H. Gong,²³ Q.B. Gou,^{1,3} M.H. Gu,^{1,3,13} F.L. Guo,¹⁶ X.L. Guo,⁶ Y.Q. Guo,^{1,3} Y.Y. Guo,¹⁴ Y.A. Han,²⁴ M. Hasan,^{1,2,3} H.H. He,^{1,2,3} H.N. He,¹⁴ J.Y. He,¹⁴ Y. He,⁶ Y.K. Hor,²⁰ B.W. Hou,^{1,2,3} C. Hou,^{1,3} X. Hou,²⁵ H.B. Hu,^{1,2,3} Q. Hu,^{12,14} S.C. Hu,^{1,3,26} D.H. Huang,⁶ T.Q. Huang,^{1,3} W.J. Huang,²⁰ X.T. Huang,²¹ X.Y. Huang,¹⁴ Y. Huang,^{1,2,3} X.L. Ji,^{1,3,13} H.Y. Jia,⁶ K. Jia,²¹ K. Jiang,^{13,12} X.W. Jiang,^{1,3} Z.J. Jiang,¹⁷ M. Jin,⁶ M.M. Kang,²⁷ I. Karpikov,¹⁰ D. Kuleshov,¹⁰ K. Kurinov,¹⁰ B.B. Li,¹¹ C.M. Li,⁷ Cheng Li,^{13,12} Cong Li,^{1,3} D. Li,^{1,2,3} F. Li,^{1,3,13} H.B. Li,^{1,3} H.C. Li,^{1,3} Jian Li,¹² Jie Li,^{1,3,13} K. Li,^{1,3} S.D. Li,^{16,2} W.L. Li,²¹ W.L. Li,⁹ X.R. Li,^{1,3} Xin Li,^{13,12} Y.Z. Li,^{1,2,3} Zhe Li,^{1,3} Zhuo Li,²⁸ E.W. Liang,²⁹ Y.F. Liang,²⁹ S.J. Lin,²⁰ B. Liu,¹² C. Liu,^{1,3} D. Liu,²¹ D.B. Liu,⁹ H. Liu,⁶ H.D. Liu,²⁴ J. Liu,^{1,3} J.L. Liu,^{1,3} M.Y. Liu,¹⁸ R.Y. Liu,⁷ S.M. Liu,⁶ W. Liu,^{1,3} Y. Liu,⁸ Y.N. Liu,²³ Q. Luo,²⁰ Y. Luo,⁹ H.K. Lv,^{1,3} B.Q. Ma,²⁸ L.L. Ma,^{1,3} X.H. Ma,^{1,3} J.R. Mao,²⁵ Z. Min,^{1,3} W. Mitthumsiri,³⁰ H.J. Mu,²⁴ Y.C. Nan,^{1,3} A. Neronov,²² L.J. Ou,⁸ P. Pattarakijwanich,³⁰ Z.Y. Pei,⁸ J.C. Qi,^{1,2,3} M.Y. Qi,^{1,3} B.Q. Qiao,^{1,3} J.J. Qin,¹² A. Raza,^{1,2,3} D. Ruffolo,³⁰ A. Sáiz,³⁰ M. Saeed,^{1,2,3} D. Semikoz,²² L. Shao,¹¹ O. Shchegolev,^{10,31} X.D. Sheng,^{1,3} F.W. Shu,³² H.C. Song,²⁸ Yu.V. Stenkin,^{10,31} V. Stepanov,¹⁰ Y. Su,¹⁴ D.X. Sun,^{12,14} Q.N. Sun,⁶ X.N. Sun,²⁹ Z.B. Sun,³³ J. Takata,³⁴ P.H.T. Tam,²⁰ Q.W. Tang,³² R. Tang,⁹ Z.B. Tang,^{13,12} W.W. Tian,^{2,19} C. Wang,³³ C.B. Wang,⁶ G.W. Wang,¹² H.G. Wang,⁸ H.H. Wang,²⁰ J.C. Wang,²⁵ Kai Wang,⁷ Kai Wang,³⁴ L.P. Wang,^{1,2,3} L.Y. Wang,^{1,3} P.H. Wang,⁶ R. Wang,²¹ W. Wang,²⁰ X.G. Wang,²⁹ X.Y. Wang,⁷ Y. Wang,⁶ Y.D. Wang,^{1,3} Y.J. Wang,^{1,3} Z.H. Wang,²⁷ Z.X. Wang,¹⁷ Zhen Wang,⁹ Zheng Wang,^{1,3,13} D.M. Wei,¹⁴ J.J. Wei,¹⁴ Y.J. Wei,^{1,2,3} T. Wen,¹⁷ C.Y. Wu,^{1,3} H.R. Wu,^{1,3} Q.W. Wu,³⁴ S. Wu,^{1,3} X.F. Wu,¹⁴ Y.S. Wu,¹² S.Q. Xi,^{1,3} J. Xia,^{12,14} G.M. Xiang,^{16,2} D.X. Xiao,¹¹ G. Xiao,^{1,3} Y.L. Xin,⁶ Y. Xing,¹⁶ D.R. Xiong,²⁵ Z. Xiong,^{1,2,3} D.L. Xu,⁹ R.F. Xu,^{1,2,3} R.X. Xu,²⁸ W.L. Xu,²⁷ L. Xue,²¹ D.H. Yan,¹⁷ J.Z. Yan,¹⁴ T. Yan,^{1,3} C.W. Yang,²⁷ C.Y. Yang,²⁵ F. Yang,¹¹ F.F. Yang,^{1,3,13} L.L. Yang,²⁰ M.J. Yang,^{1,3} R.Z. Yang,¹² W.X. Yang,⁸ Y.H. Yao,^{1,3} Z.G. Yao,^{1,3} L.Q. Yin,^{1,3} N. Yin,²¹ X.H. You,^{1,3} Z.Y. You,^{1,3} Y.H. Yu,¹² Q. Yuan,¹⁴ H. Yue,^{1,2,3} H.D. Zeng,¹⁴ T.X. Zeng,^{1,3,13} W. Zeng,¹⁷ M. Zha,^{1,3} B.B. Zhang,⁷ F. Zhang,⁶ H. Zhang,⁹ H.M. Zhang,⁷ H.Y. Zhang,^{1,3} J.L. Zhang,¹⁹ Li Zhang,¹⁷ P.F. Zhang,¹⁷ P.P. Zhang,^{12,14} R. Zhang,^{12,14} S.B. Zhang,^{2,19} S.R. Zhang,¹¹ S.S. Zhang,^{1,3} X. Zhang,⁷ X.P. Zhang,^{1,3} Y.F. Zhang,⁶ Yi Zhang,^{1,14} Yong Zhang,^{1,3} B. Zhao,⁶ J. Zhao,^{1,3} L. Zhao,^{13,12} L.Z. Zhao,¹¹ S.P. Zhao,¹⁴ X.H. Zhao,²⁵ F. Zheng,³³ W.J. Zhong,⁷ B. Zhou,^{1,3} H. Zhou,⁹ J.N. Zhou,¹⁶ M. Zhou,³² P. Zhou,⁷ R. Zhou,²⁷ X.X. Zhou,^{1,2,3} X.X. Zhou,⁶ B.Y. Zhu,^{12,14} C.G. Zhu,²¹ F.R. Zhu,⁶ H. Zhu,¹⁹ K.J. Zhu,^{1,2,3,13} Y.C. Zou,³⁴ and X. Zuo^{1,3}

(The LHAASO Collaboration)*

¹Key Laboratory of Particle Astrophysics & Experimental Physics Division & Computing Center, Institute of High Energy Physics, Chinese Academy of Sciences, 100049 Beijing, China

²University of Chinese Academy of Sciences, 100049 Beijing, China

³Tianfu Cosmic Ray Research Center, 610000 Chengdu, Sichuan, China

⁴Dublin Institute for Advanced Studies, 31 Fitzwilliam Place, 2 Dublin, Ireland

⁵Max-Planck-Institut für Kernphysik, P.O. Box 103980, 69029 Heidelberg, Germany

⁶School of Physical Science and Technology & School of Information Science and Technology, Southwest Jiaotong University, 610031 Chengdu, Sichuan, China

⁷School of Astronomy and Space Science, Nanjing University, 210023 Nanjing, Jiangsu, China

⁸Center for Astrophysics, Guangzhou University, 510006 Guangzhou, Guangdong, China

⁹Tsung-Dao Lee Institute & School of Physics and Astronomy, Shanghai Jiao Tong University, 200240 Shanghai, China

¹⁰Institute for Nuclear Research of Russian Academy of Sciences, 117312 Moscow, Russia

¹¹Hebei Normal University, 050024 Shijiazhuang, Hebei, China

¹²University of Science and Technology of China, 230026 Hefei, Anhui, China

¹³State Key Laboratory of Particle Detection and Electronics, China

¹⁴Key Laboratory of Dark Matter and Space Astronomy & Key Laboratory of Radio Astronomy, Purple Mountain Observatory, Chinese Academy of Sciences, 210023 Nanjing, Jiangsu, China

¹⁵Research Center for Astronomical Computing, Zhejiang Laboratory, 311121 Hangzhou, Zhejiang, China

- ¹⁶Key Laboratory for Research in Galaxies and Cosmology,
Shanghai Astronomical Observatory, Chinese Academy of Sciences, 200030 Shanghai, China
- ¹⁷School of Physics and Astronomy, Yunnan University, 650091 Kunming, Yunnan, China
- ¹⁸Key Laboratory of Cosmic Rays (Tibet University),
Ministry of Education, 850000 Lhasa, Tibet, China
- ¹⁹National Astronomical Observatories, Chinese Academy of Sciences, 100101 Beijing, China
- ²⁰School of Physics and Astronomy (Zhuhai) & School of Physics (Guangzhou)
& Sino-French Institute of Nuclear Engineering and Technology (Zhuhai),
Sun Yat-sen University, 519000 Zhuhai & 510275 Guangzhou, Guangdong, China
- ²¹Institute of Frontier and Interdisciplinary Science,
Shandong University, 266237 Qingdao, Shandong, China
- ²²APC, Université Paris Cité, CNRS/IN2P3, CEA/IRFU, Observatoire de Paris, 119 75205 Paris, France
- ²³Department of Engineering Physics, Tsinghua University, 100084 Beijing, China
- ²⁴School of Physics and Microelectronics, Zhengzhou University, 450001 Zhengzhou, Henan, China
- ²⁵Yunnan Observatories, Chinese Academy of Sciences, 650216 Kunming, Yunnan, China
- ²⁶China Center of Advanced Science and Technology, Beijing 100190, China
- ²⁷College of Physics, Sichuan University, 610065 Chengdu, Sichuan, China
- ²⁸School of Physics, Peking University, 100871 Beijing, China
- ²⁹Guangxi Key Laboratory for Relativistic Astrophysics,
School of Physical Science and Technology, Guangxi University, 530004 Nanning, Guangxi, China
- ³⁰Department of Physics, Faculty of Science, Mahidol University, Bangkok 10400, Thailand
- ³¹Moscow Institute of Physics and Technology, 141700 Moscow, Russia
- ³²Center for Relativistic Astrophysics and High Energy Physics,
School of Physics and Materials Science & Institute of Space Science and Technology,
Nanchang University, 330031 Nanchang, Jiangxi, China
- ³³National Space Science Center, Chinese Academy of Sciences, 100190 Beijing, China
- ³⁴School of Physics, Huazhong University of Science and Technology, Wuhan 430074, Hubei, China
- (Dated: March 27, 2024)

We present the measurements of all-particle energy spectrum and mean logarithmic mass of cosmic rays in the energy range of 0.3–30 PeV using data collected from LHAASO-KM2A between September 2021 and December 2022, which is based on a nearly composition-independent energy reconstruction method, achieving unprecedented accuracy. Our analysis reveals the position of the knee at $3.67 \pm 0.05 \pm 0.15$ PeV. Below the knee, the spectral index is found to be $-2.7413 \pm 0.0004 \pm 0.0050$, while above the knee, it is $-3.128 \pm 0.005 \pm 0.027$, with the sharpness of the transition measured with a statistical error of 2%. The mean logarithmic mass of cosmic rays is almost heavier than helium in the whole measured energy range. It decreases from 1.7 at 0.3 PeV to 1.3 at 3 PeV, representing a 24% decline following a power law with an index of $-0.1200 \pm 0.0003 \pm 0.0341$. This is equivalent to an increase in abundance of light components. Above the knee, the mean logarithmic mass exhibits a power law trend towards heavier components, which is reversal to the behavior observed in the all-particle energy spectrum. Additionally, the knee position and the change in power-law index are approximately the same. These findings suggest that the knee observed in the all-particle spectrum corresponds to the knee of the light component, rather than the medium-heavy components.

Introduction.—The energy spectrum of cosmic rays spans a wide range from 10^9 to 10^{20} eV, roughly following a power law of $dN/dE \propto E^\gamma$, where γ is the differential spectral index. Features in the spectrum correspond to changes in γ . At approximately 4 PeV, the differential spectral index changes from $\gamma \approx -2.7$ at low energies to $\gamma \approx -3.1$. This structure is referred to as the “knee” [1]. The knee as the beginning of the transition of high energy cosmic rays from galactic to extra-galactic origin is still controversial. The energy spectrum and chemical composition of cosmic rays can provide crucial clues regarding the origin, acceleration, and propagation

mechanisms of the most energetic particles in the galaxy [2, 3]. Understanding the origin of the knee in terms of the energy spectrum is often considered fundamental for determining the origin of cosmic rays. Space-borne experiments have now extended the direct measurement of the energy spectrum of proton and helium nuclei to 100 TeV [4, 5]. Because of the rapidly decreasing flux with increasing energy, measuring cosmic rays beyond 100 TeV by space-borne experiments is challenging. The data for the spectrum above a few hundred TeV are produced by ground-based large air shower arrays. The knee structure at few PeV in all-particle energy spectrum of cosmic rays has been observed by many experiments [6–15]. Ground-based indirect experiment is the only way to measure cosmic rays with energies in the knee region, while the main problem with these experiments arises from the entanglement of primary energy, composition

* hyzhang@ihep.ac.cn(H.Y. Zhang); hhh@ihep.ac.cn(H.H. He); fengcf@sdu.edu.cn(C.F. Feng)

and the high-energy hadronic interaction models used to interpret air showers. The chemical composition and high-energy hadronic interaction models dependent systematic errors in flux were a few tens of percent. Recently, some high-energy hadronic interaction models were updated based on new data from the Large Hadron Collider (LHC) at TeV energies [16, 17]. Although a single-composition energy spectrum is the most effective way for solving this problem, identifying the composition is challenging. Thus, the problem of composition dependence on energy reconstruction must be solved to measure cosmic ray energy spectra accurately.

The Large High Altitude Air Shower Observatory (LHAASO) is a ground-based air shower observatory at 4410 m above sea level in Daocheng, China [18–20]. The high altitude of the observatory enables LHAASO to measure showers with energies in the knee region close to their maxima with minimum fluctuations. It consists of three detector arrays: a kilometer square array (KM2A), a water Cherenkov detector array (WCDA), and a wide-field-of-view Cherenkov or fluorescence telescope array (WFCTA). More details about the experimental setup can be found in [19]. The array used in this measurement is the KM2A that measures electromagnetic particles (electron, positron and gamma) and muons of air showers with high precision [21] by the electromagnetic particle detectors (EDs) and muon detectors (MDs), respectively. The MD threshold for μ^\pm is about 1 GeV [22]. The detector layout is shown in Fig. S1 of the Supplemental Material [23]. The number of electromagnetic particles (N_e) and muons (N_μ) is the deposited charge by electromagnetic particles and muons expressed in units of minimum-ionizing particles. Basing on the Matthews-Heitler model [24], a new parameter, derived by summing N_e and N_μ , is used to reconstruct primary energy in a calorimetric way. This approach is insensitive to primary composition and hadronic interaction models thus is crucial for measuring accurately the energy spectrum.

Data.—Data collected by the LHAASO-KM2A from September 2021 to December 2022 are utilized for this analysis. A maximum variation of approximately 12 hPa was observed in the atmospheric pressure, resulting in a change of about 4.4% in the muon spectra, as illustrated in Figs. S2 and S3 of the Supplemental Material [23]. The constant intensity cut (CIC) method [25, 26] is employed to correct for the atmospheric pressure effect. Subsequently, the discrepancy in the number of muons under different atmospheric pressures is reduced to less than 0.6%.

The CORSIKA (v77410) air shower generator [27] with the high-energy interaction models QGSJETII-04 [16], EPOS-LHC [17] and SIBYLL-2.3d [28], is used to generate air-shower events. For the low-energy interactions the FLUKA [29] code is used. The detector response simulation is based on the Geant4 package [30], named G4KM2A [21, 31]. The simulated detector response agrees with the response of a real detector [21]. The Monte Carlo simulation is described in detail in the Sup-

plemental Material [23].

Event selection.—High-energy electromagnetic particles near shower cores can punch through the MD overburden soil, which can pollute the measurement of muons [32, 33]. In order to mitigate this effect, N_μ within a range of 40 – 200 m from the shower core is selected for analysis. To ensure consistency in the analysis, N_e within the same range of 40 – 200 m from the shower core is also taken into account. The LHAASO is located at an altitude of 4,410 m above sea level with an vertical atmospheric depth of 600 g/cm², which corresponds to the shower maxima of cosmic rays with energies in the knee region. To capture cosmic ray showers near their maxima within an energy range of 2 orders of magnitude, events are selected with zenith angles ranging from 10° to 30°, which corresponds to an atmosphere depth of 610 and 690 g/cm², respectively. It is important to note that cosmic rays of different energies reach their shower maxima at varying atmospheric depths. Further information regarding the event selection process can be found in the Supplemental Material [23]. Above 0.3 PeV, all five mass groups of cosmic ray components reach full detection efficiency, as shown in Fig. S4 of the Supplemental Material [23]. Therefore, the geometric aperture after considering core location and zenith angle selection can be derived using the following equation:

$$A_{\text{eff}} = S \int_{\theta_1}^{\theta_2} \sin\theta \cos\theta d\theta \int_0^{2\pi} d\varphi, \quad (1)$$

Here, S represents the area of the 320 – 420 m ring from the center of the KM2A, $[\theta_1, \theta_2]$ is the observed zenith range with $\theta_1=10^\circ$ and $\theta_2=30^\circ$. The geometric aperture A_{eff} is determined to be 0.16 km²sr. In this Letter, we present the all-particle energy spectrum and the mean logarithmic mass of cosmic rays based on a dataset of 7×10^7 events, covering an energy range from 0.3 to 30 PeV.

Energy reconstruction.—Basing on the Matthews-Heitler model [24], a nearly composition-independent parameter $N_{e\mu}$ is adopted to reconstruct the primary energy of cosmic rays in a calorimetric way, which is defined as follows:

$$N_{e\mu} = N_e + 2.8N_\mu \quad (2)$$

where the calculation of N_e (or N_μ) considers only the the EDs (or MDs) within 40 – 200 m from the shower axis [32]. In this Letter, the energy reconstruction formula differs slightly from the previous article [32] where quasivertical events within one energy decade were selected. Instead, the zenith angle range of 10° – 30° is chosen for cosmic rays with energy covering 2 orders of magnitude. The energy reconstruction formula used is $\log_{10}(E/\text{GeV}) = p_0 + p_1 \cdot \log_{10}(N_{e\mu})$, details can be found in the Supplemental Material [23]. Above a few hundred TeV, the correlation between $N_{e\mu}$ and the primary energy becomes nearly independent of the components as demonstrated in Fig. S5 using the QGSJETII-04 model

and the Gaisser H3a model as examples in the Supplemental Material [23]. This suggests that the composition of the cosmic rays does not significantly impact the accuracy of the energy reconstruction based on $N_{e\mu}$. The differences of parameters p_0 and p_1 in energy reconstruction formulas for different composition models (such as Gaisser H3a [34], Horandel [35], GST [36] and GSF [37]) are very small, as shown in Table S1 of the Supplemental Material [23]. Therefore, the energy reconstruction formulas for each high-energy hadronic interaction models are based on the average parameters of four composition models, as shown in Table S2 of the Supplemental Material [23]. Different hadronic interaction models result in energy reconstruction formulas with little difference, so the average one is used to reconstruct cosmic ray energy, which is $\log_{10}(E/\text{GeV}) = 2.791 + 0.993 \cdot \log_{10}(N_{e\mu})$.

All-particle energy spectrum of cosmic rays.—The core location, direction, and energy of a shower are reconstructed, and the binned flux can be calculated using the following formula

$$J(E) = \frac{\Delta N(E)}{\Delta E \cdot A_{\text{eff}} \cdot T}, \quad (3)$$

where ΔN represents the number of events per energy bin in a given time interval T , and A_{eff} represents the geometric aperture. To validate this method, simulation data are analyzed in the same way, and the results are presented in Fig. S6 of the Supplemental Material [23], which confirm that our method can reproduce all the input spectra with high accuracy.

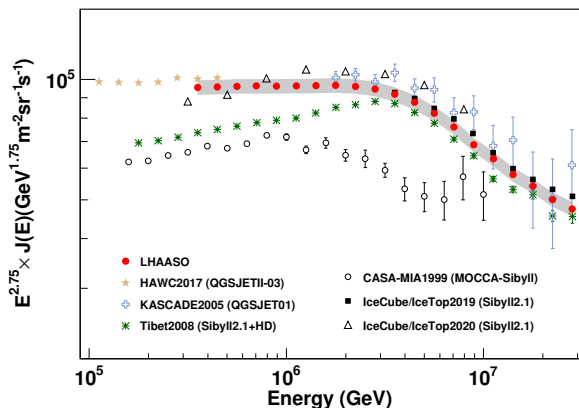


FIG. 1. The LHAASO-KM2A all-particle energy spectrum flux multiplied by $E^{2.75}$ as a function of energy. The gray shadow band represents the estimated systematic uncertainties. The results of the HAWC [38], CASA-MIA [15], Tibet-III [6], KASCADE [11], IceCube/IceTop [9, 10] are also plotted for comparison. The error bars represent the statistical uncertainties.

The all-particle energy spectrum of primary cosmic rays is calculated following Eq. (3) within the energy range of 0.3 to 30 PeV, as shown in Fig.1 from which the knee structure is clearly visible.

The systematic error of the spectrum is considered as follows. The single particle calibration uncertainty of

one ED and MD is less than 2% [39] and 0.5% [33], respectively. At 300 TeV, the average number of triggered EDs and MDs is approximately 200 and 50, respectively. Therefore, the measurement uncertainty of N_e and N_μ are both less than 0.15%, which contribute a negligible uncertainty on all-particle energy spectrum. The impact of local variations in air pressure on the results of this study is estimated to be approximately $\pm 3\%$. The systematic uncertainty observed between different composition models, such as Gaisser H3a, Horandel, GST, and GSF models, are found to be less than $\pm 1.5\%$. The influence of QGSJETII-04, EPOS-LHC, and SIBYLL-2.3d high-energy hadronic interaction models on the flux systematic uncertainty is approximately $\pm 2.5\%$ as shown in Fig. S9 of the Supplemental Material [23]. The shadow band in Fig. 1 represents the systematic uncertainties associated with air pressure, composition models, and different high-energy hadronic interaction models. A comparison of these systematic errors can be found in Table S3 of the Supplemental Material [23]. The values of the all-particle energy spectrum, along with the corresponding statistical and combined systematic uncertainties (excluding the uncertainty from hadronic interaction models), can be found in Table S5 of the Supplemental Material [23].

The AS γ experiment shows that the difference between the pure proton and pure iron primary models becomes larger in the lower energy region, where the difference in the intensities between the two models exceeds a factor of 3 at 10^{14} eV [6]. The IceTop-73 results show that the difference of energy spectrum intensities between assuming pure proton and pure iron models exceeds a factor of 1.5 at 2 PeV [40]. Of course, the extreme cases of pure proton and pure iron do not reflect reality. In this work, the flux difference between the pure proton and pure iron models is approximately 12%, which is better by more than a factor of 10 than that of previous experiments and thus allows for a more robust and reliable estimation of the primary energy of cosmic rays.

Figure 3 shows the spectrum fitted with the following formula [11, 41]

$$J(E) = \Phi_0 \cdot (E)^{\gamma_1} \left(1 + \left(\frac{E}{E_b} \right)^s \right)^{(\gamma_2 - \gamma_1)/s} \quad (4)$$

where E_b corresponds to the knee position, γ_1 and γ_2 are spectral asymptotic slopes before and after knee, s is the sharpness parameter of the knee. According to our fitting results, the knee position is at $3.67 \pm 0.05 \pm 0.15$ PeV, where the first term is statistical error and the second is systematic error. The spectral indices are $-2.7413 \pm 0.0004 \pm 0.0050$ and $-3.128 \pm 0.005 \pm 0.027$ before and after the knee, respectively. The energy spectral index changes $0.387 \pm 0.005 \pm 0.027$ before and after the knee, with the sharpness of the transition measured at $4.2 \pm 0.1 \pm 0.5$. This study represents one of the most precise measurements of the all-particle energy spectrum to date. The numerical values for different high-energy hadronic

interaction models are summarized in Table S4 of the Supplemental Material [23].

Mean logarithmic mass of cosmic rays.—According to the Matthews-Heitler model [24], the muon content of a cosmic ray shower is dependent on its composition and energy as follows:

$$N_\mu \propto A \cdot \left(\frac{E}{A \cdot \varepsilon_c} \right)^\beta \quad (5)$$

where A represents the mass of the cosmic ray, with a value of 1 for a proton and 56 for iron. Additionally, ε_c refers to the critical energy at shower maximum [42]. According to Eq. (5), given the energy, the relationship between the mean of the logarithmic muon content $\langle \ln(N_\mu) \rangle$ and the mean logarithmic mass of cosmic rays $\langle \ln(A) \rangle$ can be determined

$$\langle \ln(N_\mu) \rangle = x_0 + x_1 \cdot \langle \ln(A) \rangle. \quad (6)$$

The parameters x_0 indicate the proton $\langle \ln(N_\mu) \rangle_{\text{H}}$ and x_1 indicate $1 - \beta$ [43]. These parameters are obtained through fitting simulation data. To reduce the statistical fluctuation of the simulation data, the energy interval of the simulation data is set to 0.2, as shown in the left plot of Fig. S7 of Supplemental Material [23]. These parameters, x_0 and x_1 , exhibit variations with energy within the energy range of $\log_{10}(E_{\text{rec}}/\text{GeV}) = 5.5$ and 7.5, as shown in Fig. S7 of Supplemental Material [23] using the QGSJETII-04 model as an example. By fitting the relationship between x_0 or x_1 and cosmic ray energy, we can interpolate to obtain the corresponding values of x_0 or x_1 within a 0.1 energy interval. The validation of this method, using four assumed composition models, is illustrated in Fig. S8 of the Supplemental Material [23]. These figures confirm that our method can reproduce all the input composition models with high accuracy.

Using the above method, LHAASO measures the $\langle \ln(A) \rangle$ in each cosmic ray energy bin from 0.3 to 30 PeV, and these measurements are shown in Fig. 2, along with results from other experiments. The distribution of $\langle \ln(A) \rangle$ predicted by Gaisser H3a, Horandel, GST, and GSF models are also depicted in Fig. 2. At low energy region around 300 TeV, our results are consistent with the predictions of the Horandel, Gaisser H3a models. However, as the energy increases, our results deviate from the predictions of the Horandel or Gaisser H3a models, indicating that these models are not able to fully explain our observations.

The systematic error of the $\langle \ln(A) \rangle$ is considered as follows. The impact of local variations in air pressure on $\langle \ln(A) \rangle$ is approximately $\pm 4\%$. The differences of $\langle \ln(A) \rangle$ between several cosmic ray composition models, such as Gaisser H3a, Horandel, GST, and GSF models, are found to be less than $\pm 3\%$. The distribution of $\langle \ln(A) \rangle$ for the QGSJETII-04, EPOS-LHC, and SIBYLL-2.3d models exhibits a very similar shape, as shown in Fig. S9 of the Supplemental Material [23], and the maximum difference between them is less than $\pm 6\%$. The shadow band

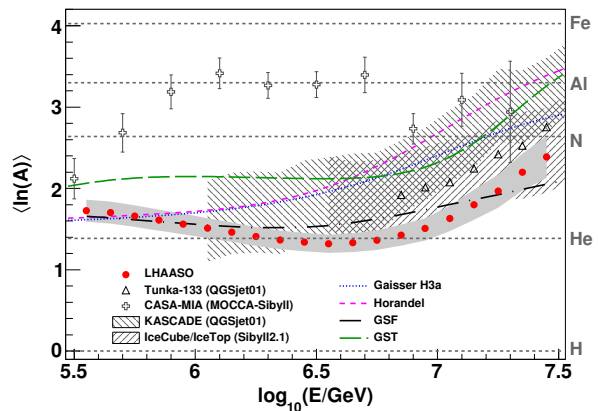


FIG. 2. The $\langle \ln(A) \rangle$ (red dots) from experimental data as a function of cosmic rays energy. The error bars show the statistical uncertainties. The gray shadow band represents the combined systematic uncertainties. The results of CASA-MIA [14] and Tunka-133 [44] are also plotted for comparison. The shadow bands represent the systematic uncertainty for KASCADE [11, 45] and IceCube/IceTop [9] experiment, respectively. The curves are the $\langle \ln(A) \rangle$ which calculated according the cosmic rays composition models.

in Fig. 2 represents the systematic uncertainties associated with air pressure, composition models, high-energy hadronic interaction models and the parameters x_0 and x_1 obtained by fitting the simulation data. The detail values of these systematic errors can be seen in Table S3 of the Supplemental Material [23]. The values of $\langle \ln(A) \rangle$, along with their corresponding statistical and combined systematic uncertainties (excluding the uncertainty from hadronic interaction models), are included in Table S6 of the Supplemental Material [23].

The results of other experiments, whose energy regions overlap with this work, are also plotted for comparison. While measurements from other experiments show a gradual increase in the mean logarithmic mass, our measurement reveals a decrease followed by an increase, with the sharpness of the transition measured at $5.5 \pm 0.3 \pm 0.9$. The systematic uncertainty of our measurement results is $\pm 9\%$, indicated by the gray shadow band in Fig. 2. In comparison, both the IceCube/IceTop experimental [9] and KASCADE [45] measurement results exhibit a systematic uncertainty of approximately $\pm 25\%$, represented by the shadow bands in Fig. 2. This study is the most precise measurement of $\langle \ln(A) \rangle$ in this energy region to date. The $\langle \ln(A) \rangle$ from different theories has been studied in [46] for the energy region from 10^{15} to 10^{17} eV. Results on $\langle \ln(A) \rangle$ from the muon content N_μ and those from the depth of shower maximum X_{max} show the same tendency toward heavier $\langle \ln(A) \rangle$ with energy beyond several PeV. Our results agree with this expectation in this energy region, where the $\langle \ln(A) \rangle$ becomes heavier with energy beyond several PeV.

The fitting results of the all-particle energy spectrum and the $\langle \ln(A) \rangle$ of the cosmic ray using Eq. (4) are shown

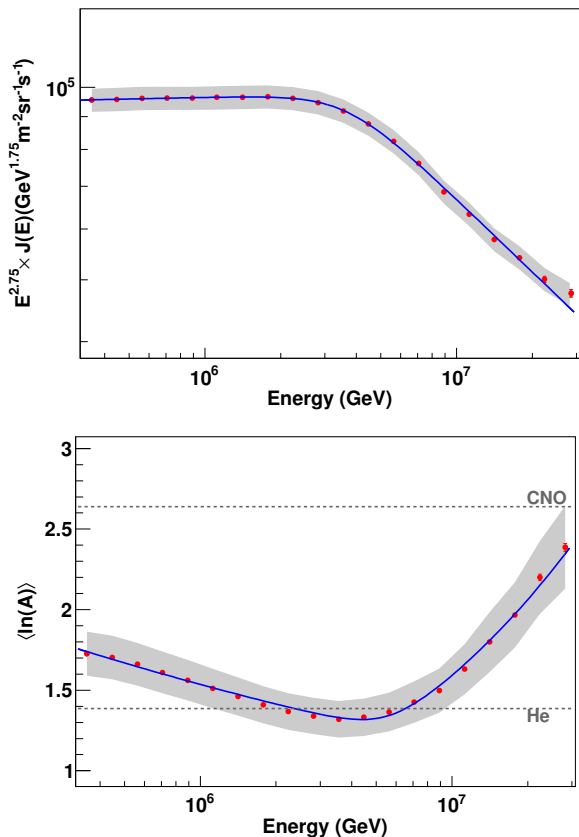


FIG. 3. Upper: The all-particle energy spectrum flux multiplied by $E^{2.75}$ as a function of energy. Bottom: The $\langle \ln(A) \rangle$ of cosmic rays as a function of energy. The error bars show the statistical uncertainties and the gray shadow band represents the estimated combined systematic uncertainties. The blue solid curves indicate the fit of Equation (4) to the data.

in Fig. 3. We find an interesting feature of the $\langle \ln(A) \rangle$ of cosmic rays: it decreases by 24% between 0.3 and 3 PeV and becomes heavier. The $\langle \ln(A) \rangle$ is closest to He [$\ln(A) = 1.39$], and lighter than CNO [$\ln(A) = 2.64$], suggesting that the first cutoff of the all-particle energy spectrum is due to light components, instead of the medium-heavy components. Another interesting feature is that the mean logarithmic mass exhibits a variation with energy, which is reversal to the behavior observed in the all-particle energy spectrum. The fitting results of $\langle \ln(A) \rangle$ has a spectral index of $\gamma_1 = -0.1200 \pm 0.0003 \pm 0.0341$ before the energy where the composition of cosmic rays shows a clear change from helium on average toward the heavier CNO on average. The corresponding change in the spectral index is $\Delta\gamma = 0.497 \pm 0.008 \pm 0.039$, occurring at an energy position of $5.36 \pm 0.08 \pm 0.46$ PeV. In our measurements, we obtained an all-particle energy spectrum index of -2.74 before the knee, while the $\langle \ln(A) \rangle$ distribution exhibits a decrease with a spectral index of -0.12 . This could be a hint that the energy spectrum index of

the light component is $[-2.74 - (-0.12)] = -2.62$ before the knee. The fit results for EPOS-LHC, QGSJETII-04 and SIBYLL-2.3d high-energy hadronic interaction models of $\langle \ln(A) \rangle$ can be found in Table S7 of the Supplemental Material [23].

Conclusions.—In this Letter, the data collected by the LHAASO-KM2A array from September 2021 to December 2022 is used to measure all-particle energy spectrum of cosmic rays from 0.3 to 30 PeV. A composite variable $N_{e\mu}$, combining the number of electromagnetic particles and muons, is weakly dependent on the composition mass of cosmic rays and is used to reconstruct the shower energy. The knee of the primary energy spectrum is observed around $3.67 \pm 0.05 \pm 0.15$ PeV with a change of index $\approx 0.387 \pm 0.005 \pm 0.027$. The combined systematic uncertainties caused by air pressure, composition models, and high-energy hadronic interaction models are approximately $\pm 4.5\%$. The difference between the pure proton and pure iron assumption models is approximately 12%.

The $\langle \ln(N_\mu) \rangle$ in cosmic rays air showers with energies from 0.3 to 30 PeV is measured by KM2A detectors. The relationship between $\langle \ln(N_\mu) \rangle$ and $\langle \ln(A) \rangle$ of cosmic rays is studied using the simulation data with EPOS-LHC, QGSJETII-04 and SIBYLL-2.3d as high-energy hadronic interaction models. The $\langle \ln(A) \rangle$ exhibits a variation with energy, which is reversal to the behavior observed in the all-particle energy spectrum. The derived $\langle \ln(A) \rangle$ becomes heavier after several PeV. The distribution of $\langle \ln(A) \rangle$ suggests that the first cutoff of the all-particle energy spectrum is light components, not the medium-heavy components. The combined systematic uncertainties, which include air pressure, composition models, the uncertainty of the parameters x_0 and x_1 obtained by fitting and high-energy hadronic interaction models are approximately $\pm 9\%$.

We would like to thank all staff members who work at the LHAASO site above 4400 meters above sea level year round to maintain the detector and keep the water recycling system, electricity power supply and other components of the experiment operating smoothly. We are grateful to Chengdu Management Committee of Tianfu New Area for the constant financial support for research with LHAASO data. This research work is also supported by the following grants: The National Key R & D program of China under Grants No. 2018YFA0404201, No. 2018YFA0404202 and No. 2018YFA0404203, No. 2018YFA0404204, by the National Natural Science Foundation of China (NSFC No.12022502, No.12205314, No. 12105301, No. 12261160362, No.12105294, No.U1931201, No.12175121, No.12275280). We are grateful to the Institute of Plateau Meteorology, CMA Chengdu to maintain meteorological data, and in Thailand by the National Science and Technology Development Agency (NSTDA) and the National Research Council of Thailand (NRCT) under the High-Potential Research Team Grant Program (N42A650868). We are particularly grateful to Dr. L. Q. Yin for the cross-check.

- [1] G. Kulikov and G. Khristiansen, On the size spectrum of extensive air showers, *Sov. Phys. JETP* **35**, 441 (1959).
- [2] J. R. Hörandel, Models of the knee in the energy spectrum of cosmic rays, *Astropart. Phys.* **21**, 241 (2004).
- [3] B. D. Piazzoli *et al.*, Chapter 4 Cosmic-Ray Physics, *Chin. Phys. C* **46**, 030004 (2022).
- [4] Q. An *et al.* (DAMPE Collaboration), Measurement of the cosmic ray proton spectrum from 40 GeV to 100 TeV with the DAMPE satellite, *Sci. Adv.* **5**, eaax3793 (2019).
- [5] Y. S. Yoon *et al.* (CREAM Collaboration), Proton and Helium Spectra from the CREAM-III Flight, *Astrophys. J.* **839**, 5 (2017).
- [6] M. Amenomori *et al.* (Tibet AS γ Collaboration), The All-Particle Spectrum of Primary Cosmic Rays in the Wide Energy Range from 10^{14} to 10^{17} eV Observed with the Tibet-III Air-Shower Array, *Astrophys. J.* **678**, 1165 (2008).
- [7] A. TAMBURRO, MEASUREMENTS OF COSMIC RAYS WITH ICETOP/ICECUBE: STATUS AND RESULTS, *Mod. Phys. Lett. A* **27**, 1230038 (2012).
- [8] M. G. Aartsen *et al.* (IceCube Collaboration), Measurement of the cosmic ray energy spectrum with IceTop-73, *Phys. Rev. D* **88**, 042004 (2013).
- [9] M. G. Aartsen *et al.* (IceCube Collaboration), Cosmic ray spectrum and composition from PeV to EeV using 3 years of data from IceTop and IceCube, *Phys. Rev. D* **100**, 082002 (2019).
- [10] M. G. Aartsen *et al.* (IceCube Collaboration), Cosmic ray spectrum from 250 TeV to 10 PeV using IceTop, *Phys. Rev. D* **102**, 122001 (2020).
- [11] T. Antoni *et al.*, KASCADE measurements of energy spectra for elemental groups of cosmic rays: Results and open problems, *Astropart. Phys.* **24**, 1 (2005).
- [12] J. C. Arteaga-Velázquez (KASCADE-Grande Collaboration), Measurements of the muon content of EAS in KASCADE-Grande compared with SIBYLL 2.3 predictions, *Proc. Sci. ICRC2017*, 316 (2017).
- [13] S. Berezhnev *et al.* (Tunka Collaboration), The Tunka-133 EAS Cherenkov light array: Status of 2011, *Nucl. Instrum. Methods Phys. Res., Sect. A* **692**, 98 (2012), 3rd Roma International Conference on Astroparticle Physics.
- [14] M. Glasmacher *et al.*, The cosmic ray composition between 10^{14} and 10^{16} eV, *Astropart. Phys.* **12**, 1 (1999).
- [15] M. Glasmacher *et al.*, The cosmic ray energy spectrum between 10^{14} and 10^{16} eV, *Astropart. Phys.* **10**, 291 (1999).
- [16] S. Ostapchenko, QGSJET-II: physics, recent improvements, and results for air showers, *EPJ Web Conf.* **52**, 02001 (2013).
- [17] T. Pierog *et al.*, EPOS LHC: Test of collective hadronization with data measured at the CERN Large Hadron Collider, *Phys. Rev. C* **92**, 034906 (2015).
- [18] Z. Cao (LHAASO Collaboration), A future project at tibet: the large high altitude air shower observatory (LHAASO), *Chin. Phys. C* **34**, 249 (2010).
- [19] H. H. He (LHAASO Collaboration), Design of the LHAASO detectors, *Radiat. Detect. Technol. Methods* **2** (2018).
- [20] X.-H. Ma *et al.*, Chapter 1 LHAASO Instruments and Detector technology, *Chin. Phys. C* **46**, 030001 (2022).
- [21] F. Aharonian *et al.* (LHAASO Collaboration), Observation of the Crab Nebula with LHAASO-KM2A - a performance study, *Chin. Phys. C* **45**, 025002 (2021).
- [22] C. Li *et al.* (LHAASO Collaboration), Measurement of muonic and electromagnetic components in cosmic ray air showers using LHAASO-KM2A prototype array, *Phys. Rev. D* **98**, 042001 (2018).
- [23] See Supplemental Material at <http://link.aps.org/supplemental/10.1103/PhysRevLett.132.131002> for the validation of methods, measured fluxes and systematic uncertainties, and the results of spectral fitting.
- [24] J. Matthews, A heitler model of extensive air showers, *Astropart. Phys.* **22**, 387 (2005).
- [25] J. Hersil *et al.*, Observations of Extensive Air Showers near the Maximum of Their Longitudinal Development, *Phys. Rev. Lett.* **6**, 22 (1961).
- [26] W. Apel *et al.*, Probing the evolution of the EAS muon content in the atmosphere with KASCADE-Grande, *Astropart. Phys.* **95**, 25 (2017).
- [27] D. Heck and T. Pierog, Extensive Air Shower Simulation with CORSIKA: A User's Guide, (Karlsruher Institut für Technologie, Karlsruhe, Germany, 2021) .
- [28] F. Riehn *et al.*, Hadronic interaction model sibyll 2.3d and extensive air showers, *Phys. Rev. D* **102**, 063002 (2020).
- [29] G. Battistoni *et al.*, Overview of the FLUKA code, *Ann. Nucl. Energy* **82**, 10 (2015).
- [30] S. Agostinelli *et al.*, GEANT4-a simulation toolkit, *Nucl. Instrum. Methods Phys. Res., Sect. A* **506**, 250 (2003).
- [31] S. Z. Chen *et al.*, Design of the Detector Simulation of LHAASO-KM2A, *Nucl. Electron. Detect. Technol.* **37**, 1101 (2017).
- [32] H. Y. Zhang, H. H. He, and C. F. Feng, Approaches to composition independent energy reconstruction of cosmic rays based on the LHAASO-KM2A detector, *Phys. Rev. D* **106**, 123028 (2022).
- [33] X. Zuo *et al.*, Design and performances of prototype muon detectors of lhaaso-km2a, *Nucl. Instrum. Methods Phys. Res., Sect. A* **789**, 143 (2015).
- [34] T. K. Gaisser *et al.*, Cosmic ray energy spectrum from measurements of air showers, *Front. Phys.* **8**, 748 (2013).
- [35] Jörg R. Hörandel, On the knee in the energy spectrum of cosmic rays, *Astropart. Phys.* **19**, 193 (2003).
- [36] T. Stanev *et al.*, High energy cosmic rays: sources and fluxes, *Nucl. Instrum. Methods Phys. Res., Sect. A* **742**, 42 (2014), 4th Roma International Conference on Astroparticle Physics.
- [37] H. Dembinski *et al.*, Data-driven model of the cosmic-ray flux and mass composition from 10 GeV to 10^{11} GeV, *Proc. Sci. ICRC2017*, 533 (2017).
- [38] R. Alfaro *et al.* (HAWC Collaboration), All-particle cosmic ray energy spectrum measured by the HAWC experiment from 10 to 500 TeV, *Phys. Rev. D* **96**, 122001 (2017).
- [39] F. Aharonian *et al.* (LHAASO Collaboration), Self-calibration of lhaaso-km2a electromagnetic particle detectors using single particles within extensive air showers, *Phys. Rev. D* **106**, 122004 (2022).
- [40] M. G. Aartsen *et al.* (IceCube Collaboration), Measurement of the cosmic ray energy spectrum with icetop-73, *Phys. Rev. D* **88**, 042004 (2013).

- [41] S. V. Ter-Antonyan and L. S. Haroyan, About EAS size spectra and primary energy spectra in the knee region (2000), [arXiv:hep-ex/0003006 \[hep-ex\]](#).
- [42] J. Alvarez-Muñiz *et al.*, Hybrid simulations of extensive air showers, [Phys. Rev. D **66**, 033011 \(2002\)](#).
- [43] H. Dembinski, Computing mean logarithmic mass from muon counts in air shower experiments, [Astropart. Phys. **102**, 89 \(2018\)](#).
- [44] S. Berezhnev *et al.*, The Tunka-133 EAS Cherenkov light array: Status of 2011, [Nucl. Instrum. Methods Phys. Res., Sect. A **692**, 98 \(2012\)](#).
- [45] K.-H. Kampert and M. Unger, Measurements of the cosmic ray composition with air shower experiments, [Astropart. Phys. **35**, 660 \(2012\)](#).
- [46] H. P. Dembinski *et al.*, Report on Tests and Measurements of Hadronic Interaction Properties with Air Showers, [EPJ Web Conf. **210**, 02004 \(2019\)](#).